

Fluorescence Fluctuation Spectroscopy Enables Quantification of Potassium Channel Subunit Dynamics and Stoichiometry

Giulia Tedeschi

University of California, Irvine

Lorenzo Scipioni

University of California, Irvine

Maria Papanikolaou

University of California, Irvine

Geoffrey Abbott

University of California, Irvine

Michelle Digman (✉ mdigman@uci.edu)

University of California, Irvine

Research Article

Keywords: Voltage-gated potassium (Kv), plasma membrane, KCNE, protein diffusion, stoichiometry

Posted Date: December 10th, 2020

DOI: <https://doi.org/10.21203/rs.3.rs-121439/v1>

License:  This work is licensed under a Creative Commons Attribution 4.0 International License.

[Read Full License](#)

Fluorescence Fluctuation Spectroscopy enables quantification of potassium channel subunit dynamics and stoichiometry

Giulia Tedeschi^{1†}, Lorenzo Scipioni^{1†}, Maria Papanikolaou², Geoffrey W. Abbott^{2*}, Michelle A. Digman^{1*}

¹ Department of Biomedical Engineering, Laboratory for Fluorescence Dynamics, University of California Irvine, Irvine, CA 92697, USA.

² Department of Physiology and Biophysics, Bioelectricity Laboratory, School of Medicine, University of California Irvine, Irvine, CA 92697, USA.

Corresponding authors:

*Dr. Geoffrey W. Abbott

Department of Physiology and Biophysics, Bioelectricity Laboratory, School of Medicine, University of California Irvine, Irvine, CA 92697, USA.

Email: abbottg@uci.edu **Phone:** 949 824 3269

*Dr. Michelle A. Digman

Department of Biomedical Engineering, Laboratory for Fluorescence Dynamics, University of California Irvine, Irvine, CA 92697, USA.

Email: mdigman@uci.edu **Phone:** 949 824 3255

[†]These authors contributed equally to this work.

ABSTRACT

Voltage-gated potassium (Kv) channels are a family of membrane proteins that facilitate K⁺ ion diffusion across the plasma membrane, regulating both resting and action potentials. Kv channels comprise four pore-forming α subunits, each with a voltage sensing domain, and they are regulated by interaction with β subunits such as those belonging to the KCNE family. Here we conducted a comprehensive biophysical characterization of stoichiometry and protein diffusion across the plasma membrane of the epithelial KCNQ1-KCNE2 complex, combining total internal reflection fluorescence (TIRF) microscopy and a series of complementary Fluorescence Fluctuation Spectroscopy (FFS) techniques. Using this approach, we found that KCNQ1-KCNE2 has a predominant 4:4 stoichiometry, while non-bound KCNE2 subunits are mostly present as dimers in the plasma membrane. At the same time, we identified unique spatio-temporal diffusion modalities and nano-environment organization for each channel subunit. These findings improve our understanding of KCNQ1-KCNE2 channel function and suggest strategies for elucidating the subunit stoichiometry and forces directing localization and diffusion of ion channel complexes in general.

Introduction

Potassium ion (K⁺) channels are a numerous and diverse class of membrane proteins that facilitate passage of K⁺ across biological membranes by creating an environment conducive to selective, gated yet rapid passive diffusion down the electrochemical gradient. In higher animals, the two largest classes of K⁺ channels are the voltage-gated potassium (Kv) channels and the two-pore domain potassium (K2P) channels. Kv channels comprise four α subunits each containing a pore module attached to a voltage-sensing domain (VSD); the assembled tetramer contains a single, central pore. Kv channels are opened by depolarization of the cell membrane, a voltage shift sensed by the VSD, that results in a conformational shift which is communicated to the pore which in turn opens. Kv channels are therefore essential for setting action potential shape, frequency and morphology, and their action is required for action potential repolarization and thus the ability to fire trains of action potentials. K2P channels, formed in contrast from dimers of subunits, can remain open at resting voltages and thereby contribute substantially to setting resting membrane potential of many cell types. Kv channels and K2P channels are structurally distinct but exhibit some functional overlap. K2P channels lack the classic VSD but may exhibit non-canonical voltage-gating behavior. By the same token, a small subset of Kv channels can lose or greatly shift their voltage dependence, becoming constitutively active at resting

membrane potentials. This property enables them to serve roles in non-excitable cells, such as epithelial cells. The prime example is the KCNQ1 (Kv7.1) α subunit. Homomeric KCNQ1 channels are voltage-gated and closed at resting membrane potential. However, KCNQ1 homomers likely do not play a major role in native K^+ currents. Instead, KCNQ1 partners with β subunits of the KCNE family to produce a range of currents important in native cellular physiology¹.

The KCNE subunits are single-pass transmembrane β subunits best known for modifying the functional properties of voltage-gated potassium (Kv) channel α subunits in the auditory epithelium, other epithelia, auditory neurons, and cardiac myocytes. Each of the five human KCNE subunits can regulate multiple different Kv channel α subunits, typically forming heteromeric complexes with unique functional attributes compared to those of other subunit compositions. In addition, many of the forty known Kv α subunits in the human genome are regulated by more than one KCNE isoform. This leads to an impressive potential combinatorial complexity¹⁻⁴. While KCNQ1-KCNE1 complexes retain their voltage-dependence, albeit their gating is slowed and other attributes changed compared to homomeric KCNQ1, co-assembly of KCNQ1 with KCNE2 or KCNE3 exerts more dramatic influence. KCNE2 regulates KCNQ1 in the gastric, thyroid, choroid plexus and pancreatic epithelia, typically enabling function of various ions and other solute transporters. KCNE3 regulates KCNQ1 in the colon epithelium, where the complex provides a basal K^+ flux to regulate cAMP-stimulated chloride ion secretion, and probably in mammary epithelium. All these tasks require persistent (non-inactivating) K^+ flux at negative membrane potentials, a feature not typically associated with Kv channels. Accordingly, KCNE2 and KCNE3 each convert KCNQ1 to a constitutively active K^+ channel, facilitating the above essential functions¹. The past 25 years have yielded a wealth of knowledge surrounding the importance of KCNE-based potassium channels in cells and tissues including auditory epithelia, auditory neurons, other epithelia, and cardiac myocytes. More recently, investigators have made important breakthroughs using high-resolution spectroscopy, cryo-electron microscopy and modeling to elucidate the structure, binding sites and mechanisms of action of KCNEs within Kv channel complexes⁵⁻⁸. Despite these studies, some fundamental questions regarding the molecular composition and subunit dynamics of KCNE complexes remain either controversial or incompletely addressed. These questions often lie in the middle ground between high resolution structure and cell biology.

Here, focusing on the KCNQ1-KCNE2 complex that is essential for normal gastric, thyroid and choroid plexus function, we employed a toolbox of complementary imaging and biophysical analysis techniques to probe heteromeric channel stoichiometry and subunit dynamics, designed to cover the entire spatial and temporal resolution required for a full picture of dynamic processes which are responsible for the formation of different complexes. Given the different expression levels and the diverse functional effects depending on the binding with specific subunits, it is not known how these complexes are regulated at the nanometer scale and what is the role of the nano-environment organization. A technique capable of measuring the modality and rate of lateral diffusion, stoichiometry and size of the confinement regions is needed to observe subtle changes in channels behavior by considering multiple parameters at the same time. Various methods used for studying these complexed proteins enabled observation of dynamic interactions between pairs of protein, e.g.. Förster resonance energy transfer (FRET) experiments. However, this method is restricted to protein pairs and can be influenced by factors such as dipole alignment and the local microenvironment. Advanced biophysical approaches, such as temporal fluctuation analysis, bypass the limitation of protein pairs and exploits the contribution of the variance of intensity fluctuations that reveals the distribution of higher oligomeric states in each pixel of an image. This method, the Number and Molecular Brightness (N&B) analysis, can be used to analyze image sequences acquired from laser scanning microscopes⁹ or camera based systems¹⁰. The advantage of this data is that the same image sequences can also be used to calculate the various types of protein mobility, diffusion rates of molecules and routes adopted by molecules at short- and long-range distances, using complementary fluorescence fluctuations-based approaches. For this work, fluorescence microscopy datasets were acquired with a total internal reflection (TIRF, **Figure 1A**) microscope, which enables selective imaging of the plasma membrane of living cells, and the same dataset was analyzed with a combination of state-of-the-art fluorescence fluctuation spectroscopy (FFS) techniques. FFS techniques can be variously used to obtain important biophysical parameters such as protein size and concentration¹¹⁻¹³, lateral diffusion coefficient¹⁴⁻¹⁶ and diffusion modality^{16,17}, spatiotemporal heterogeneity in FRET^{18,19} and have also been applied in combination with super-resolution techniques²⁰⁻²². In this work, we applied image-derived mean square displacement^{23,24} (iMSD, **Figure 1B**), 2D pair correlation function²⁵ (2D-pCF, **Figure 1C**) and number and brightness analysis^{9,10} (N&B, **Figure 1D**). These techniques allowed us to simultaneously obtain information about the organization of the nano-environment (iMSD), the protein directionality (2D-pCF) and oligomerization state (N&B) of the KCNQ1-KCNE2 complex. To better understand the dynamic properties of this potassium channel we performed our experiments by transfecting CHO cells with one of the subunits (meGFP-tagged) or co-transfecting with both of them (meGFP-, mCherry-tagged).

Our results reveal that the KCNE2 subunit shows either fast ($>0.02\mu\text{m}^2\text{s}^{-1}$) or slow ($<0.02\mu\text{m}^2\text{s}^{-1}$) micro-diffusion as well as increased diffusive eccentricity when co-expressed with KCNQ1 at short ranges ($\sim 220\text{nm}$).

The nanodomain confinement size for the fast population matched that of KCNQ1 suggesting that this population may represent heteromeric KCNE2-KCNQ1 complex whereas the slow diffusive population represents the unbound KCNE2. The N&B analysis confirmed homodimers of KCNE2 proteins in the absence of KCNQ1 and tetramers upon binding to KCNQ1. Overall, we describe a model for KCNE2 with respect to KCNEQ1 dynamic interactions at nanometer scale using advanced fluorescence fluctuation analysis.

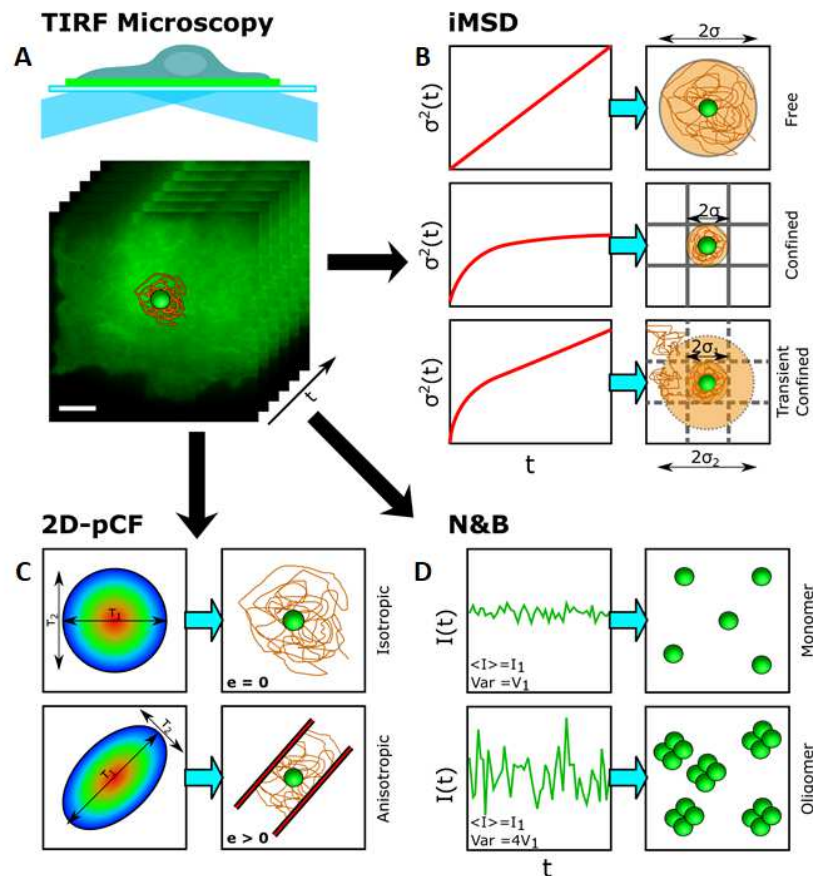


Figure 1: Schematic representation of the imaging and analysis approach. **A:** Image sequences are acquired using a TIRF microscope. **B:** Representative iMSD curves for different diffusion models (left) and their interpretation including free, confined and transient confined motions (right). **C:** Example of local 2D pair correlation functions, 2D- pCF, (left) and their interpretation of either isotropic or anisotropic diffusion (right). **D:** Temporal fluorescence fluctuation intensities for different oligomerization states (left) and their interpretation (right) obtained from Number and Brightness analysis.

Results and Discussion

Fluorescent-tagged KCNQ1-KCNE2 channels exhibit normal channel activity.

KCNQ1 α subunits each contain 6 transmembrane segments, S1-S6, organized into a VSD (S1-S4) and a pore module (S5-S6). We modified the human KCNQ1 cDNA such that the protein was C-terminally tagged with monomeric enhanced Green Fluorescent Protein (meGFP). KCNE2 is a single transmembrane segment β subunit; we C-terminally tagged the human KCNE2 gene with genetically encoded mCherry (**Figure 2A**). There are no high-resolution structures or structural models for KCNQ1-KCNE2 channels. However, the Sanders group generated a high-resolution model of KCNQ1-KCNE1⁵, showing KCNE1 in a crevice between the VSD of one KCNQ1 α subunit and the pore module of a neighboring KCNQ1 α subunit (**Figure 2B**). Previous stoichiometry studies argue for between two and four KCNE1 subunits in a KCNQ1-KCNE1 complex^{6,7}. Using cryo-electron microscopy, the Mackinnon group solved the high-resolution structure of KCNQ1-KCNE3 channels with PIP₂ and calmodulin bound⁸. The structure shows a tetramer of α subunits and four KCNE3 β subunits, positioned again between the VSD and pore modules of neighboring subunits (**Figure 2C**). Here, we first expressed KCNQ1-meGFP alone or with KCNE2-mCherry in Chinese Hamster Ovary (CHO

cells) and recorded the currents generated using a standard voltage clamp protocol, with whole-cell patch clamp electrophysiology. KCNQ1-meGFP expressed voltage-dependent currents with similar properties to those we and others previously observed for untagged KCNQ1, including a “hook” in the -30 mV tail current that indicates recovery from inactivation²⁶. Also similar to previous observations for untagged KCNQ1-KCNE2 channels, KCNQ1-meGFP/KCNE2-mCherry channels were constitutively active, expressing smaller currents than homomeric KCNQ1-meGFP (**Figure 2D, E**) and with flat -30 mV tail currents indicative of minimal voltage dependence and an absence of inactivation (**Figure 2F**). Thus, the fluorescent tags used in this study did not noticeably perturb KCNQ1-KCNE2 electrical activity.

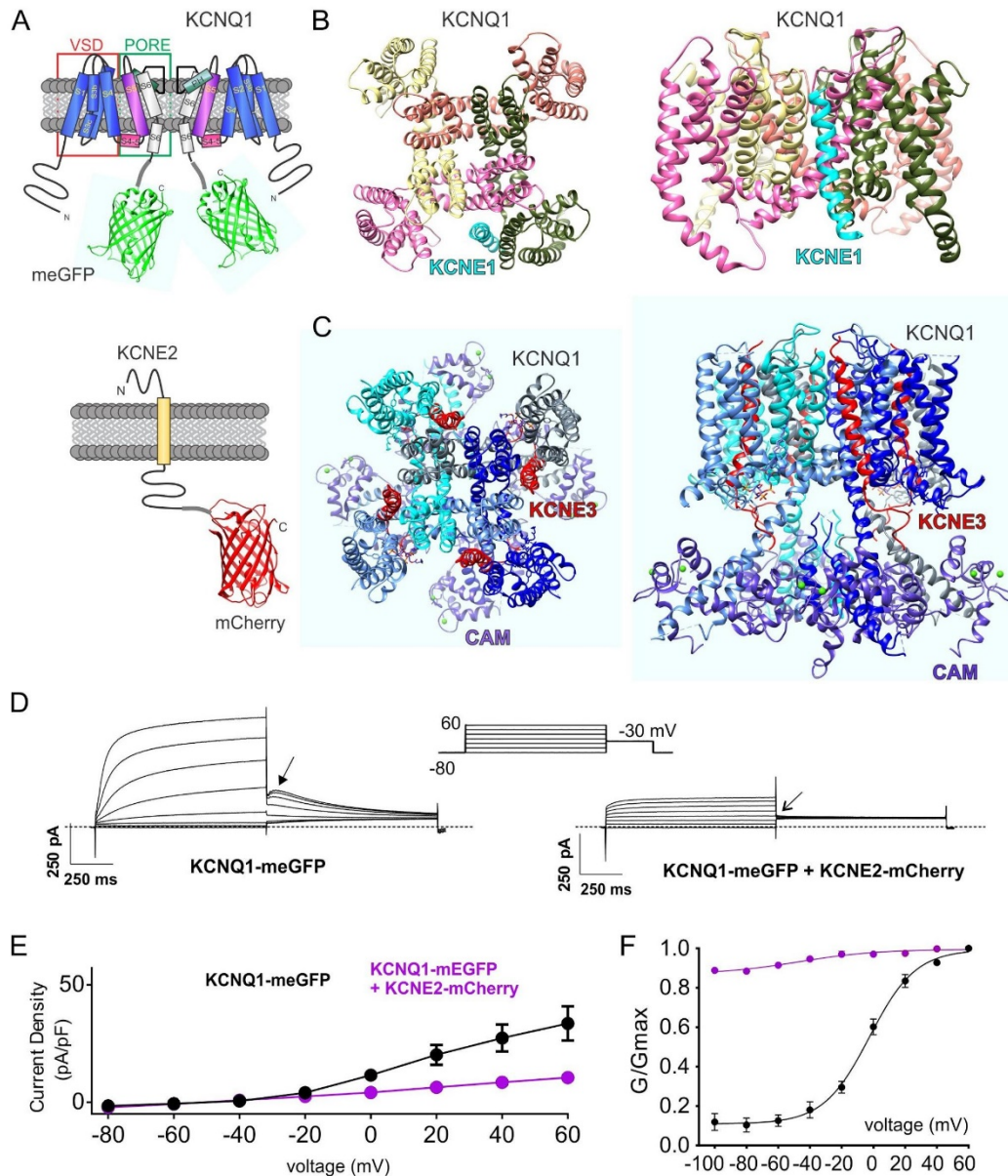


Figure 2: Fluorescent-tagged KCNQ1 and KCNQ1-KCNE2 express normal currents. **A:** Transmembrane topologies of KCNQ1 and KCNE2 subunits showing fluorescent protein tagging of the cytosolic domains. **B:** Extracellular (left) and intramembrane (right) views of structural model of KCNQ1-KCNE1 complex⁵. **C:** Extracellular (left) and intramembrane (right) views of cryo-electron microscopy-resolved structure of KCNQ1-PIP2-KCNE3-calmodulin complex⁸. CAM = calmodulin. **D:** Exemplary traces showing whole-cell patch-clamp recordings from CHO cells transfected with the subunit combinations shown. Dotted line indicates zero current level. Upper inset shows the voltage protocol. Arrows indicate tail current features. **E:** Mean prepulse current density \pm SEM for currents expressed by KCNQ1-meGFP alone (black) ($n = 14$) or with KCNE2-mCherry (purple) ($n = 12$). **F:** Mean G/G_{max} relationship \pm SEM measured from tail currents at arrows in panel D for currents expressed by KCNQ1-meGFP alone (black) ($n = 14$) or with KCNE2-mCherry (purple) ($n = 12$).

iMSD provides dynamic fingerprinting of the nano-environment

Lateral modes of mobility at the plasma membrane can significantly impact protein signaling²⁷. To this end, we applied the iMSD analysis, which exploits spatiotemporal fluorescence fluctuations caused by protein diffusion to obtain various types of protein mobility reported by the iMSD^{23,24} curve. This curve can be used to define the diffusion model of a molecule and measure important biophysical parameters to obtain a dynamic picture of proteins diffusing in their nano-environment. iMSD is a particularly powerful technique since it yields similar information as single particle tracking (SPT)²⁸ but is not limited by the need to visualize single molecules. This property allows to extend its applicability to more physiologically relevant applications and to a much larger range of protein concentration. From the iMSD analysis, we were able to determine that the diffusion modality which best describes the dynamic behavior of the proteins in the nano-environment was transiently confined diffusion for all the conditions considered, i.e. expressed independently or co-expressed (summarized in **Table 1**), as shown in the example in **Figure 3 A-B**. The parameters obtained from fitting this model are the size of the domains in which the protein is diffusing (length of confinement, L_{conf}) as well as the diffusion coefficient inside (micro-diffusion coefficient, D_{micro}) and across (macro-diffusion coefficient, D_{macro}) the nano-domains. The micro-diffusion coefficient distribution, in particular, revealed two distinct populations for the KCNE2 when co-expressed with the KCNQ1: approximately 46% of the cells analyzed displayed a D_{micro} slower than $0.02 \mu\text{m}^2\text{s}^{-1}$, $E2_s(Q1)$, while the rest displayed a faster diffusing population, $E2_f(Q1)$. Given this distinct behavior, we separated the cells displaying the fast and the slow micro-diffusion in order to further investigate this finding. In **Figure 3 C-E** we show the distribution of the parameters obtained from the iMSD analysis. After separating the slow and fast components for the $E2(Q1)$, a clear difference in behavior between the two populations can be appreciated in the length of confinement, where the $E2_f(Q1)$ has the same size of the nano-domains as the Q1 samples. This observation led us to the hypothesis that the $E2_f(Q1)$ is the population that binds to the Q1 channel, whereas the $E2_s(Q1)$ represents the unbound component. The macro-diffusion of the $E2_f(Q1)$ and $E2_s(Q1)$ is similar to that of KCNE2 without KCNQ1 co-expression and different from the Q1 samples. We attribute this result to membrane-localized KCNE2 subunits that are not bound to KCNQ1, again suggesting the ability of KCNE2 to reach the plasma membrane alone. Whether or not the KCNE2 subunits can dynamically bind on and off KCNQ1 tetramers while in the plasma membrane remains uncertain.

Acronym	Proteins (co-)expressed
E2	KCNE2 - meGFP
E2(Q1)	KCNE2 - meGFP / KCNQ1 - mCherry
Q1	KCNQ1 - meGFP
Q1(E2)	KCNQ1 - meGFP / KCNE2 - mCherry
GAP	GAP-meGFP

Table 1: Summary of the experiment conditions and related terminology used throughout the paper.

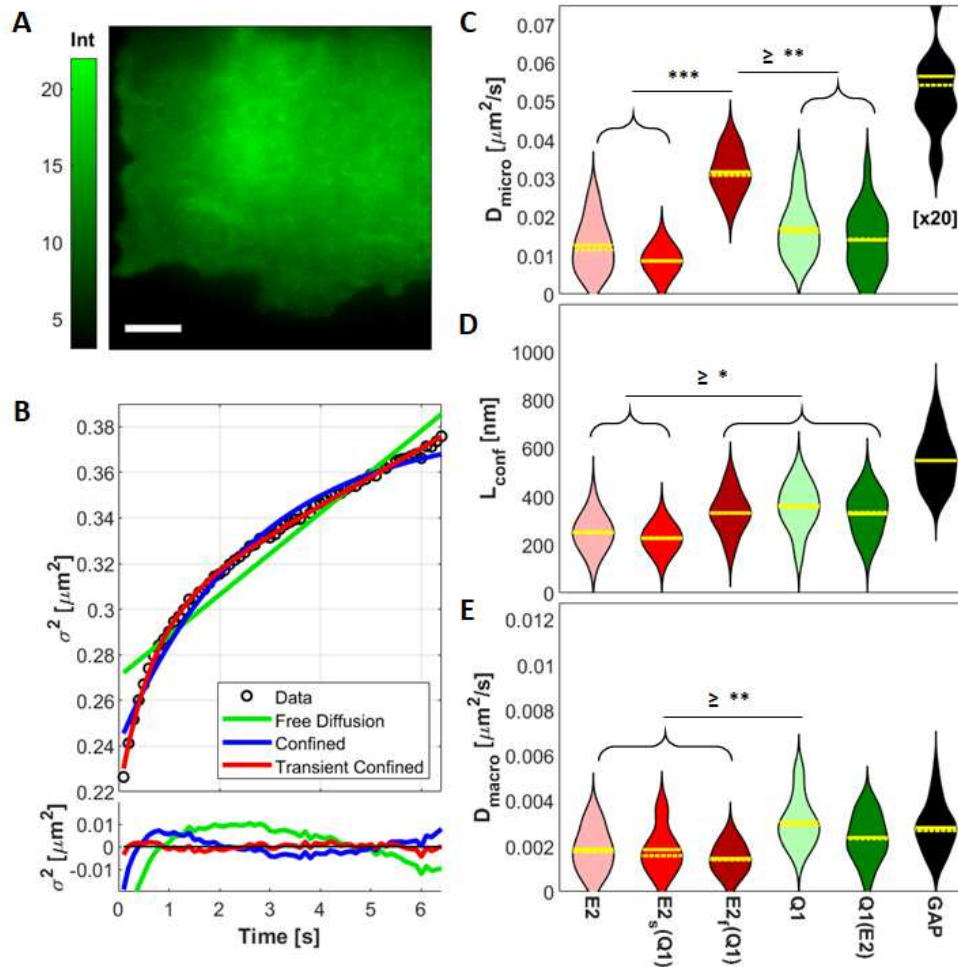


Figure 3: Representative average intensity image (A) and iMSD analysis (B) of a CHO cell transfected with KCNE2-meGFP. iMSD curve (B, top) fitted with three different diffusion models and their residuals (B, bottom). Violin plots of the parameters obtained from the fitting with a transient confined model: D_{micro} (C), L_{conf} (D) and D_{macro} (E) for the samples considered. Scale bar in A is $5 \mu\text{m}$. Solid and dashed yellow lines represent the mean and the median of the distributions, respectively. Asterisks represent p -values <0.05 (*), <0.01 (**) and <0.001 (***).

Directionality of diffusion for KCNQ1 and KCNE2

Sensitivity to diffusion obstacles and their spatial organization can be an important factor affecting voltage channels functionality. For instance, lateral diffusion of sodium channels in the axons has been shown to modulate receptor concentrations and may regulate neuronal plasticity²⁹. To understand if KCNQ1 or KCNE2 protein complexes experience diffusion barriers and if these interactions are unique to each complex, we used the 2D-pCF analysis²⁵, which has the capability of mapping barriers to diffusion^{29–32}. Briefly, if a diffusing protein encounters an obstacle, its diffusion will no longer be isotropic but it will preferentially diffuse away from that obstacle. In our data, this behavior is represented by the eccentricity, which describes whether the protein is diffusing isotropically ($e = 0$) or anisotropically ($e > 0$). Eccentricity can be measured at different distances and in **Figure 4** we show the eccentricity as a function of the distance for the conditions considered, together with representative fluorescence intensity images and eccentricity maps. Our results show that the KCNQ1 channel displays a very low eccentricity, comparable with that of our inert control membrane bound form of the meGFP (GAP-meGFP). KCNE2 generally shows a higher eccentricity, which significantly increases at short range (220 nm) for the E2_f(Q1). Furthermore, from the 2D-pCF images it is possible to spatially map the localization of binding loci at the membrane for both the KCNQ1 and the KCNE2, which appear as rings of high eccentricity³⁰. Since CHO cells are not polarized and do not display any distinctive spatial feature (e.g. the axon in neurons), we considered the overall median eccentricity of the whole cell. However, the capability to assess the spatial distribution of binding loci can have far-reaching applications if used for instance in combination with fluorescently labeled structural components of the membrane.

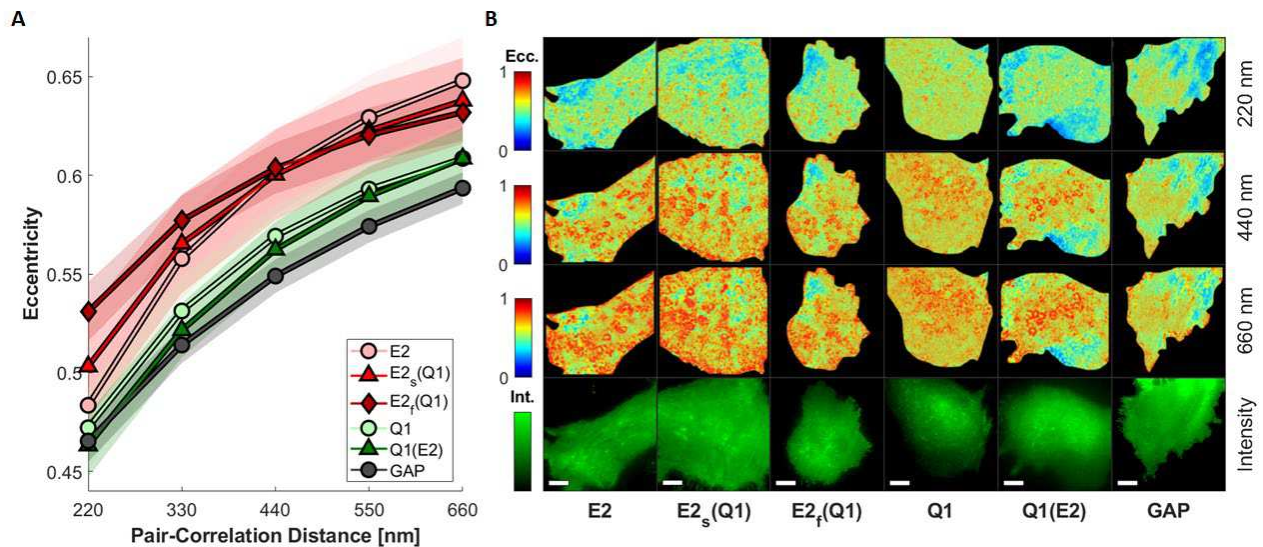


Figure 4: Median eccentricity as a function of the pCF distance considered (A), shaded areas represent the 95% confidence interval. B: Representative 2D-pCF eccentricity images computed at different distances and relative intensity images (bottom). Scale bar is 5 μm.

Number and Brightness analysis of KCNQ1-KCNE2 stoichiometry

We applied N&B analysis to measure the oligomerization state of the complex subunits and to further examine the differences between E2_s(Q1) and E2_f(Q1) (Figure 5). First, we found that the KCNE2 subunit exists on the membrane in the form of a dimer in the absence of KCNQ1 co-expression (Figure 5A). Our finding that KCNE2 reaches the plasma membrane when expressed alone, and forms homodimers in this environment, is in agreement with previous observations that non-fluorescent-tagged KCNE2 is able to traffic alone to the cell surface³³. This observation is in contrast, however, with some prior findings for non-tagged KCNE1, which was reported to be unable to reach the cell surface alone³⁴. Others reported that the fluorescent-tagged KCNE1 is capable of solo surface expression in *Xenopus laevis* oocytes⁶; the source of this discrepancy is not known, but possible explanations are that the tag may alter trafficking, or that endogenous KCNQ1 in oocytes was taking KCNE1 to the membrane. The KCNE2 regulatory subunit was previously found to traffic to the surface of HEK293 cells much more efficiently than KCNE1 or the hERG alpha subunit with which KCNE1 and KCNE2 can interact. Furthermore, KCNE2 was even found to be secreted into the extracellular medium. Importantly, KCNE2 proteins with the correct mass for dimers were detected in the extracellular fraction by western blot and confirmed by mass spectrometry analysis as being KCNE2 homodimers and the higher mass confirmed as not arising from glycosylation³³. The dimeric form of KCNE2 reported by Um and McDonald was not tagged with a fluorescent molecule, supporting the premise that dimerization in our study is intrinsic to KCNE2 and not an artifact of tagging. In the current study, using N&B, upon KCNQ1 co-expression, the E2_f(Q1) results indicated four E2 subunits per KCNQ1-KCNE2 complex, whereas the E2_s(Q1) suggested on average three E2 subunits (Figure 5A). Since the trimeric form is not thought to be a physiological configuration, we interpreted our result as stemming from a mixture of dimeric (unbound) and tetrameric (KCNQ1-bound) forms of KCNE2. In this scenario, the slow micro-diffusion we measure for the E2_s(Q1) is predominantly driven by the unbound dimeric population, although a small population of bound tetrameric KCNE2 is measured in the N&B analysis. Further indications to support the hypothesis that the E2_f(Q1) represents the component bound to the KCNQ1 is the fact that the cells assigned to the E2_f(Q1) show a higher expression level of the KCNQ1 with respect to KCNE2 (Figure 5B, center), compared to the E2_s(Q1). N&B analysis of the KCNQ1 describes the complex as tetrameric with or without co-expression with KCNE2 (Figure 5A and C). Importantly, from our data we could not correlate any dependence of the oligomerization state on the expression level (Figure 5B-C), although it was reported elsewhere for KCNQ1-KCNE1 by some⁶ but not others⁷.

While the current study represents to our knowledge the first assessment of KCNQ1-KCNE2 channel stoichiometry, a number of studies have been conducted on related channels, primarily KCNQ1-KCNE1 (I_{Ks}) complexes. Initial studies from the Goldstein lab, each employing different counting techniques (site-directed mutagenesis with macroscopic or microscopic functional analysis, and toxin binding), indicated a probable 4:2 KCNQ1-KCNE1 subunit stoichiometry, although the possibility of 4:4 was not entirely dismissed. The rigid 4:2

stoichiometry was also arrived at in a later study using a chemically releasable irreversible inhibitor. The Goldstein lab then subsequently utilized counting of fluorescent tag bleaching to further reinforce the idea of 4:2 KCNQ1-KCNE1 subunit stoichiometry and effectively rule out, in their hands, variable stoichiometry^{7,35,36}. However, other labs have contended that they observe a variable stoichiometry with up to 4 KCNE1 subunits per channel complex, depending on KCNE1 expression levels relative to KCNQ1, based on single molecule fluorescence bleaching⁶. More recently, the MacKinnon lab solved a structure of KCNQ1-KCNE3 complexes using cryo-electron microscopy, and found a 4:4 stoichiometry⁸. In addition, using photobleaching, the Felipe lab recently counted 4:4 for KCNA3:KCNE4, although they too reported a variable KCNE4 stoichiometry in the complexes depending on the relative expression level, and concluded that functional attributes varied with stoichiometry³⁷. Finally, using photobleaching, the D'Avanzo group concluded that complexes formed by pacemaker (HCN) channel alpha subunit and KCNE2, which may contribute to pacemaking in the heart and/or brain, have an expression-level dependent variable stoichiometry of between 4:1 and 4:4 (HCN:KCNE2)³⁸.

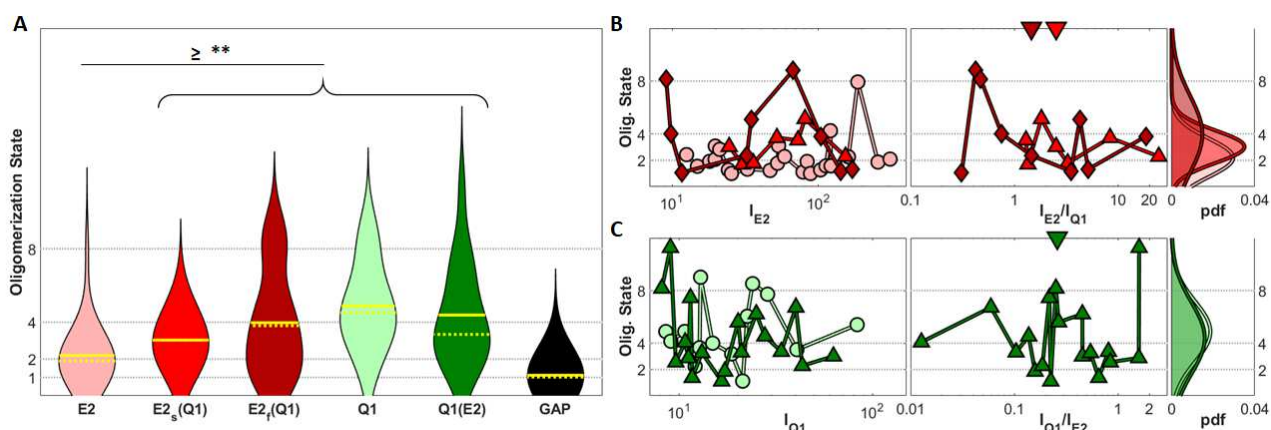


Figure 5: Violin plot for the oligomerization state as obtained by N&B analysis (A) for the samples considered. Dependence of the oligomerization state for the KCNE2-meGFP (B) and KCNQ1-meGFP (C) samples with the expression (left, represented by the average intensity of the meGFP channel) or co-expression (center, represented as the ratio between the average intensity of the meGFP and the mCherry channels) level, together with the corresponding probability density functions (right). Downward facing triangles in B and C represent the median co-expression level. Asterisks represent p -values <0.05 (*), <0.01 (**) and <0.001 (***). Colors and markers are the same as in Figure 4.

Dynamic fingerprinting and nanoscale model of the KCNQ1-KCNE2 complex.

To compare the biophysical and dynamic characteristics of KCNE2 and KCNE1 alone or in complexes between them, we combined all the information of oligomerization and diffusion properties obtained by our multiplexed analysis and represented them in the form of a spider plot (Figure 6A-B). This plot can provide an immediate quantification of the biophysical properties we can measure with our FFS-based approach. We used this plethora of information to create a graphic model of the membrane environment and homo- and hetero-oligomerization state of the proteins considered for this study (Figure 6C). A complete table of the parameters used is available in the Supplementary Information. In our model, the confinement regions are represented as square microdomains with size equal to L_{conf} , the micro- and macro-diffusion as a circular region with diameter $d = \sqrt{4Dt}$ where t is 0.5 s for D_{micro} and 60 s for D_{macro} . Directionality is represented as two ellipses with eccentricity equal to the eccentricity calculated from 2D-pCF at a distance of 220 nm (inner ellipse) and 660 nm (outer ellipse). KCNQ1 and KCNE2 are represented with their oligomerization state measured from N&B and colored according to the appropriate fluorescent protein tagging. As shown pictorially by the dark blue circle in each panel, KCNE2 dimers diffuse slower and travel a shorter distance than when bound to tetramers of KCNQ1 ($E2_t(Q1)$), approximately 150–200 nm and 300 nm in 0.5 s, respectively. When KCNE2 dimers are bound to tetramers of KCNQ1, two populations of distinct diffusions emerge as shown in Figure 3. There are no notable differences in diffusion for complexes of KCNQ1 when bound or not bound to KCNE2.

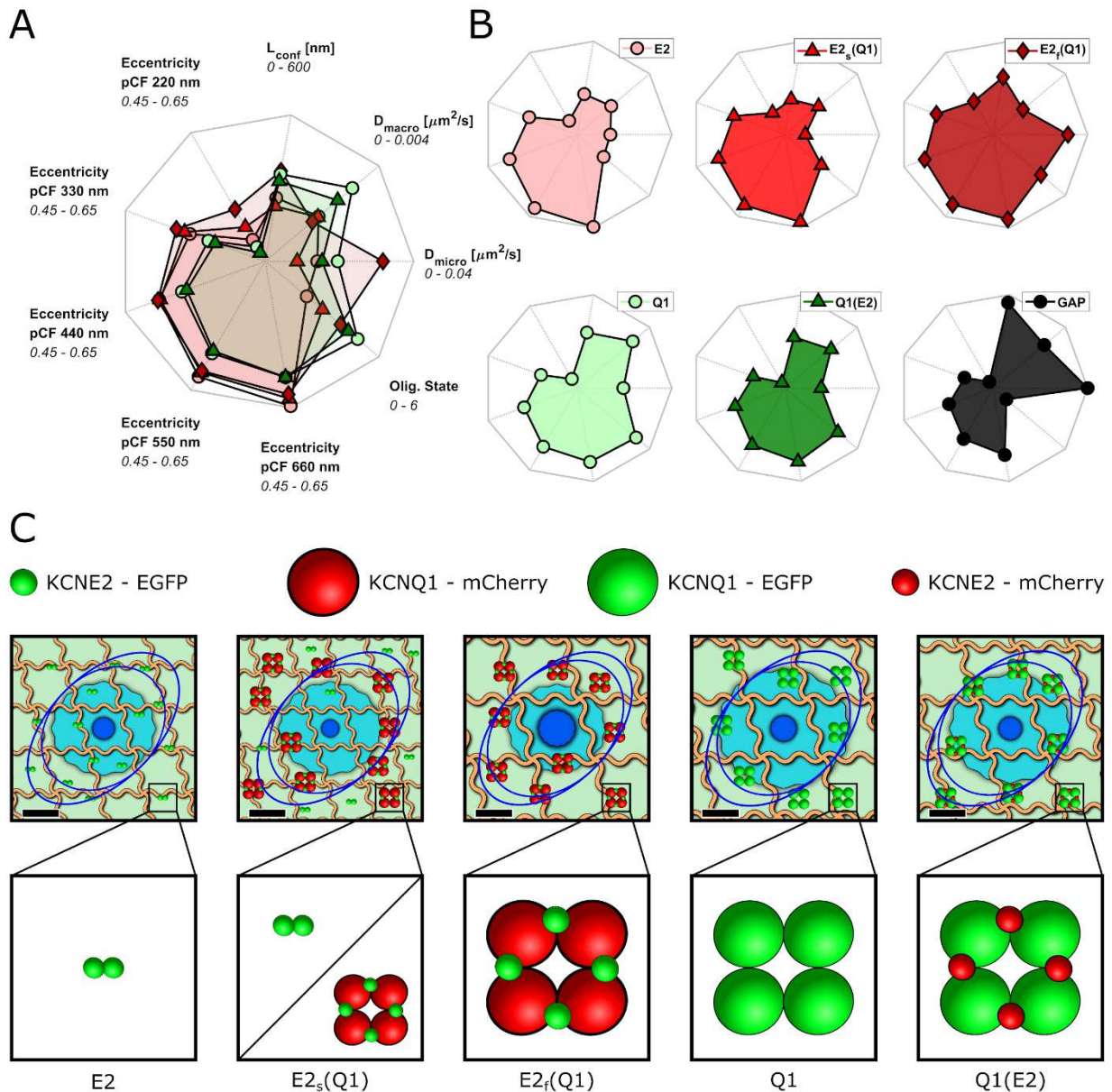


Figure 6: Combined (A) and individual (B) spider plots for all the conditions considered. C: Comprehensive schematic representation of the diffusional nano-environment together with the model of the oligomerization state for the KCNQ1-KCNE2 complex. Scale bar for the model is 200 nm and proteins are shown 10x their actual size. The dark blue and light blue circles represent the area covered by the diffusion of the protein in 0.5 s (calculated from D_{micro}) and 60 s (calculated from D_{macro}), respectively. Orange lines represent the nano-domains and the blue ellipses show the eccentricity as short scale (220 nm, internal ellipse) and long scale (660 nm, external ellipse).

Conclusions

A wide variety of KCNQ-KCNE complexes likely exist *in vivo*, as tetramers of the KCNQ1 alpha subunit can co-assemble with each of the five KCNE ancillary subunit isoforms, with diverse functional consequences, and it is thought that, for example, native KCNQ1 channels always incorporate one or more of the KCNE isoforms. Further, KCNEs serve broad roles extending beyond direct regulation of Kv channel electrical attributes, including modulating other types of ion channel, and also regulating features of Kv channel biology beyond their electrical attributes - such as trafficking, α subunit composition, and regulation by other proteins and by ions and small molecules including drugs, protons and PIP_2 ^{2-4,39,40}. Studies of *Kcne* knockout (*Kcne*^{-/-}) mice have uncovered crucial and diverse KCNE activities, and predicted disorders that were subsequently linked to human gene disruption⁴¹⁻⁴⁹. In addition, human *KCNE* gene variants are implicated in life-threatening inherited

or acquired human disorders. These include cardiac rhythm disturbances such as Long QT syndrome (LQTS), Brugada Syndrome (BrS) and atrial fibrillation (AF)⁵⁰. *Kcne* germline knockout mice exhibit syndromes compatible to those in humans as well as additional ones not yet recognized in human populations. Examples of the former include the inherited arrhythmia syndromes mentioned above and also the recent discovery of an unexpected link between KCNE2 and coronary artery disease in people^{51,52} and in mice⁵³. As an example of the latter, *Kcne2* gene deletion in mice causes a multisystem syndrome predisposing to sudden cardiac death that includes multiple risk factors for coronary artery disease, such as diabetes, elevated serum LDL and angiotensin II, fatty liver and also anemia^{43,54,55}. Some of the features of this KCNE2-linked multisystem pathology have been recognized in human populations^{51,52}. *Kcne2* deletion also causes hypothyroidism, achlorhydria and increased seizure susceptibility in mice^{45,47,56}.

Reflecting the disease states described above, KCNE2 is essential for the normal function of a variety of epithelia and also has important roles in the heart and brain in at least some species². In epithelia, the primary partner for KCNE2 is KCNQ1. KCNQ1-KCNE2 channel complexes are required for gastric acid secretion, normal thyroid hormone production, normal choroid plexus physiology and regulation of *myo*-inositol regulation in the cerebrospinal fluid, and normal pancreatic beta-cell activity^{45,47,56,57}. All of the above underscores the importance of understanding all aspects of KCNQ1-KCNE2 channel biology, including channel stoichiometry and subunit dynamics. Our findings herein that KCNQ1-KCNE2 likely exist as octamers containing four of each subunit can guide our understanding of how these physiologically important channels function. Furthermore, given their role in several diverse, highly specialized cell types, the enhanced understanding of their movement within the cell membrane produced by this study can be built upon to understand the forces directing and localizing KCNQ1 and KCNE2 subunits in the various polarized cell types in which they are expressed - perturbation of which *in vivo* has been shown to contribute to complex disease states^{46,48,49}.

The biophysical methods used in this work reveal the types of translational motion of molecules at the plasma membrane. Since the biophysical properties of both membrane organization and protein dynamics vary extensively across temporal and spatial scales, it is important to study the diffusion pattern which is dynamically kept out of equilibrium as cells tend to continuously regulate ion channel trafficking⁵⁸. We showed that our multiplexed methods, and in particular iMSD and 2D-pCF analyses, can extract complex diffusion behaviors (Brownian diffusion, confinement/hopping dynamics) without the need to visualize single molecules, greatly simplifying sample preparation and analysis and providing unbiased and user-independent results while avoiding perturbing the correct functionality of the channels, as shown from our electrophysiology results. Furthermore, the N&B method provides information on the oligomerization state of the diffusing proteins, making the approach presented in this study ideal for a system of such complexity. In general, our use of TIRF imaging, a powerful yet relatively common technology, in combination with a series of Fluorescence Fluctuation Spectroscopy techniques allows researchers to determine, in a single acquisition, the oligomerization state, the diffusion modality and the nano-environment organization, making our approach generally suitable for a larger variety of applications in more than one field.

Materials and Methods

Cell culture and transfection for whole cell patch-clamp.

We seeded CHO cells (ATCC) onto poly-L-lysine treated glass coverslips and transfected using TransIT-LT1 (Mirus Bio LLC, Madison, WI, USA) the following day with CMV-based expression constructs containing cDNA for human KCNE2 (C-terminally mCherry-tagged), and/or KCNQ1 (C-terminally mGFP-tagged). Cells were cultured in DMEM with 10% FBS and 1% penicillin/streptomycin in a 95% O₂/5% CO₂ humidified environment at 37°C for 48-72 hours post transfection prior to patch-clamping. We purchased cell culture consumables and reagents from VWR or Fisher Scientific unless otherwise stated.

Whole-cell Patch Clamp

We recorded currents expressed in CHO cell using whole-cell patch-clamp at room temperature (22-25°C) with 3-6 MΩ borosilicate glass electrodes backfilled with solution containing (in mM): 90 K Acetate, 20 KCl, 40 HEPES, 3 MgCl₂, 1 CaCl₂, 3 EGTA-KOH, 2 MgATP; pH7.2. We perfused cells continuously at 1-2ml/min with an extracellular solution containing (in mM): 135 NaCl, 5 KCl, 5 HEPES, 1.2 MgCl₂, 2.5 CaCl₂, 10 glucose; pH 7.4. We purchased chemicals from Fisher Scientific or Sigma-Millipore. We held cells at -80mV in voltage clamp before applying the voltage step protocols and recording currents in response to pulses between -80 mV and +40 or +60 mV at 20 mV intervals, followed by a single pulse to -30 mV, using a CV -7A Headstage (Axon Instruments, Foster City, CA, USA). Currents were amplified using a Multi-clamp 700B (Axon

Instruments), low-pass filtered at 2-10 kHz using an eight-pole Bessel filter and digitization was achieved (sampling at 10-40 kHz) through a DigiData 1322A interface (Molecular Devices; Sunnyvale, CA). We used pClamp8 (Molecular Devices) Clampex software for data acquisition and Clampfit software for analysis, together with Graphpad Prism 7.0 (Graphpad; La Jolla, CA, USA).

Cell culture and transfection for imaging.

CHO (ATCC) cells were cultured in low glucose medium (Ham's F-12K Medium Kaighn's modification, Gibco, ThermoFisher Scientific), supplemented with 10% v/v Fetal Bovine Serum (Heat Inactivated FBS, GenClone, Genesee) and 1% v/v Penicillin/Streptomycin Solution 100X (10,000 units of penicillin and 10mg/mL streptomycin in 0.85% saline solution, GenClone, Genesee), in a 37°C and 5% CO₂ incubator. One day before transfection, cells were seeded in 35mm glass bottom dishes (MatTek Corporation), previously coated with 2µg/mL Fibronectin in Dulbecco's Phosphate Buffer Solution (Fibronectin human plasma 0.1% solution, Sigma-Aldrich), DPBS 1X without Ca, Mg, Phenol Red, GenClone, Genesee). CMV-based expression constructs containing cDNA for C-terminally meGFP-tagged or mCherry-tagged human KCNE2 or KCNQ1 were used for single or co-transfections. For calibration, cells were transfected with GAP-meGFP plasmid (pCAG-meGFP was a gift from Connie Cepko, Addgene plasmid #14757; <http://n2t.net/addgene:14757>; RRID:Addgene_14757). Transfections were performed with Lipofectamine 3000 Kit (Invitrogen, ThermoFisher Scientific) diluted in Opti-MEM I reduced-serum medium (Gibco, ThermoFisher Scientific), according to manufacturer instruction. Approximately one day after transfection, Opti-MEM medium was substituted with culture medium (low glucose medium supplemented with 10% v/v Fetal Bovine and 1% v/v Penicillin/Streptomycin Solution 100X). Cells were maintained in the incubator (37°C and 5% CO₂) prior to fluorescence microscopy experiments (48 hrs after transfection).

Total Internal Reflection Fluorescence (TIRF) Microscopy.

Fluorescence measurements were acquired with an Olympus IX83 TIRF. The system is equipped with a stagetop incubation system (Tokai Hit) providing CO₂, humidity and temperature control. Temperature was maintained at 37°C and CO₂ at 5%. Samples were excited with a 491nm laser (Olympus) for meGFP or a SuperK Evo White Light Laser (NKT Photonics) with excitation filter 560/15 (Chroma) for mCherry and focused by a UAPO N 100x/1.49 NA Oil objective (Olympus). TIRF angle was set by software to achieve a penetration depth of 110 nm, corresponding to a TIRF angle of 67.91° for the 491 nm line and 69.45° for the 560 nm line. The fluorescence signal was separated by a 560 longpass dichroic beam splitter mounted on an Optosplit II (Cairn) and the two bands were collected by a Prime 95B sCMOS camera (Photometrics). Co-transfected samples were sequentially excited with the appropriate lasers. For the meGFP channel, 1050 frames were acquired with 100 ms integration time, whereas for the mCherry channel 128 frames were acquired with 100 ms integration time. Laser power was set at 10 % (green) and 60 % (red) for all measurements. The microscope was controlled by Micromanager 1.4 (ImageJ). A sample of Tetraspeck fluorescent beads (100 nm diameter) were used to calibrate the point spread function waist and for fluorescence channels registration.

Analysis

The number of cells analyzed for each condition is listed in the following table

<i>Experiment</i>	<i>Number of cells</i>
E2	23
E2 _s (Q1)	12
E2 _i (Q1)	14
Q1	22
Q1(E2)	23
GAP	74

2D-pCF

2D-pCF analysis was performed with SimFCS 4 (Globals). For each cell a user-defined mask was obtained and used in the analysis. Sampling parameters such as pixel size (55nm), frame time (100ms) and point spread function waste (210nm) were entered in the program. 2D-pCF analysis was performed at 4, 6, 8, 10, 12 pixel distance.

iMSD

iMSD analysis was performed with a custom code written in MATLAB. From a user-defined rectangular region the spatiotemporal ACF, represented by a 3D matrix, was computed. Each XY plane of this matrix was fitted to a two-dimensional Gaussian function and the $\sigma^2(t)$ was stored and fitted with a free diffusion, confined and transient confined as described elsewhere²²⁻²⁴.

N&B

Number and brightness analysis was performed with a custom code written in MATLAB. The mean and variance along the temporal dimension of the image stack was computed and the brightness was obtained after correcting for the dark noise/offset and the gain of the camera, as described elsewhere^{10,22,59}. The brightness of the monomers was found to increase linearly with the average intensity; therefore, we performed a fitting of the brightness of all the monomers acquired as a function of the average intensity. The resulting function was used to obtain the oligomerization state for the experiments, scaled with the appropriate average intensity value.

Statistical analysis

Electrophysiology

All values are expressed as mean \pm SEM. Students' t-test was used for statistical comparisons. All P-values were two-sided. Statistical significance was defined as $P < 0.05$.

FFS

Distributions are represented with violin plots using the MATLAB function "Hoffmann H, 2015: violin.m - Simple violin plot using matlab default kernel density estimation. INRES (University of Bonn), Katzenburgweg 5, 53115 Germany." Bandwidth was set as 0.0033 (**Figure 3C**), 53.33 (**Figure 3D**), 0.0005 (**Figure 3E**) and 1.5 (**Figure 5A**). Students' t-test was used for statistical comparisons. All P-values were two-sided. Statistical significance is shown as asterisks corresponding to p-values < 0.05 (*), < 0.01 (**) and < 0.001 (***). All distributions have been tested for normality. Complete diagrams of statistical significance are shown in the **Supplementary Figures**.

Author Contributions

GWA and MAD conceived the original idea ,GT and LS carried out FFS experiments and analysis, MP carried out electrophysiology experiments. The manuscript was written through contributions of all authors. All authors have given approval to the final version of the manuscript.

Acknowledgments

This work was supported by the National Institutes of Health, National Institute of Deafness and Communication Disorders under Grant R21DC015736 to GWA, MAD, GT, and MP; National Institute of General Medical Sciences under Grant R35GM130377 to GWA; and NIH P41-GM103540 grant to LS and MAD.

Competing interests

The authors declare no competing interests.

Data availability

The datasets generated during and/or analyzed during the current study are available from the corresponding authors on reasonable request.

References

1. Abbott, G. W. Biology of the KCNQ1 Potassium Channel. *New J. Sci.* (2014). doi:10.1155/2014/237431
2. Abbott, G. W. The KCNE2 K⁺ channel regulatory subunit: Ubiquitous influence, complex pathobiology. *Gene* (2015). doi:10.1016/j.gene.2015.06.061
3. Abbott, G. W. KCNE1 and KCNE3: The yin and yang of voltage-gated K⁺ channel regulation. *Gene* (2016). doi:10.1016/j.gene.2015.09.059
4. Abbott, G. W. KCNE4 and KCNE5: K⁺ channel regulation and cardiac arrhythmogenesis. *Gene* (2016). doi:10.1016/j.gene.2016.07.069
5. Kang, C. *et al.* Structure of KCNE1 and implications for how it modulates the KCNQ1 potassium channel. *Biochemistry* (2008). doi:10.1021/bi800875q
6. Nakajo, K., Ulbrich, M. H., Kubo, Y. & Isacoff, E. Y. Stoichiometry of the KCNQ1 - KCNE1 ion channel complex. *Proc. Natl. Acad. Sci. U. S. A.* (2010). doi:10.1073/pnas.1010354107
7. Plant, L. D., Xiong, D., Dai, H. & Goldstein, S. A. N. Individual IKs channels at the surface of mammalian cells contain two KCNE1 accessory subunits. *Proc. Natl. Acad. Sci. U. S. A.* (2014). doi:10.1073/pnas.1323548111
8. Sun, J. & MacKinnon, R. Structural Basis of Human KCNQ1 Modulation and Gating. *Cell* (2020). doi:10.1016/j.cell.2019.12.003
9. Digman, M. A., Dalal, R., Horwitz, A. F. & Gratton, E. Mapping the number of molecules and brightness in the laser scanning microscope. *Biophys. J.* (2008). doi:10.1529/biophysj.107.114645
10. Unruh, J. R. & Gratton, E. Analysis of molecular concentration and brightness from fluorescence fluctuation data with an electron multiplied CCD camera. *Biophys. J.* (2008). doi:10.1529/biophysj.108.130310
11. Scipioni, L., Gratton, E., Diaspro, A. & Lanzanò, L. Phasor Analysis of Local ICS Detects Heterogeneity in Size and Number of Intracellular Vesicles. *Biophys. J.* **111**, 619–629 (2016).
12. Wiseman, P. W. Image correlation spectroscopy: Principles and applications. *Cold Spring Harb. Protoc.* (2015). doi:10.1101/pdb.top086124
13. Wiseman, P. W., Squier, J. A., Ellisman, M. H. & Wilson, K. R. Two-photo image correlation spectroscopy and image cross-correlation spectroscopy. *J. Microsc.* (2000). doi:10.1046/j.1365-2818.2000.00736.x
14. Digman, M. A. & Gratton, E. Fluorescence correlation spectroscopy and fluorescence cross-correlation spectroscopy. *Wiley Interdiscip. Rev. Syst. Biol. Med.* (2009). doi:10.1002/wsbm.5
15. Rossow, M. J., Sasaki, J. M., Digman, M. A. & Gratton, E. Raster image correlation spectroscopy in live cells. *Nat. Protoc.* (2010). doi:10.1038/nprot.2010.122
16. Veerapathiran, S. & Wohland, T. The imaging FCS diffusion law in the presence of multiple diffusive modes. *Methods* (2018). doi:10.1016/j.ymeth.2017.11.016
17. Digiacoio, L., Digman, M. A., Gratton, E. & Caracciolo, G. Development of an image Mean Square Displacement (iMSD)-based method as a novel approach to study the intracellular trafficking of nanoparticles. *Acta Biomater.* (2016). doi:10.1016/j.actbio.2016.07.031
18. Liang, Z., Lou, J., Scipioni, L., Gratton, E. & Hinde, E. Quantifying nuclear wide chromatin compaction by phasor analysis of histone Förster resonance energy transfer (FRET) in frequency domain fluorescence lifetime imaging microscopy (FLIM) data. *Data Br.* (2020). doi:10.1016/j.dib.2020.105401
19. Lou, J. *et al.* Phasor histone FLIM-FRET microscopy quantifies spatiotemporal rearrangement of chromatin architecture during the DNA damage response. *Proc. Natl. Acad. Sci. U. S. A.* (2019). doi:10.1073/pnas.1814965116
20. Honigsmann, A. *et al.* Scanning STED-FcS reveals spatiotemporal heterogeneity of lipid interaction in the plasma membrane of living cells. *Nat. Commun.* (2014). doi:10.1038/ncomms6412
21. Lanzanò, L. *et al.* Measurement of nanoscale three-dimensional diffusion in the interior of living cells by STED-FCS. *Nat. Commun.* (2017). doi:10.1038/s41467-017-00117-2
22. Scipioni, L., Lanzanó, L., Diaspro, A. & Gratton, E. Comprehensive correlation analysis for super-resolution dynamic fingerprinting of cellular compartments using the Zeiss Airyscan detector. *Nat. Commun.* (2018). doi:10.1038/s41467-018-07513-2
23. Di Rienzo, C., Gratton, E., Beltram, F. & Cardarelli, F. Fast spatiotemporal correlation spectroscopy to determine protein lateral diffusion laws in live cell membranes. *Proc. Natl. Acad. Sci. U. S. A.* (2013). doi:10.1073/pnas.1222097110
24. Rienzo, C. Di, Gratton, E., Beltram, F. & Cardarelli, F. From fast fluorescence imaging to molecular diffusion law on live cell membranes in a commercial microscope. *J. Vis. Exp.* (2014). doi:10.3791/51994

25. Di Rienzo, C., Cardarelli, F., Di Luca, M., Beltram, F. & Gratton, E. Diffusion Tensor Analysis by Two-Dimensional Pair Correlation of Fluorescence Fluctuations in Cells. *Biophys. J.* (2016). doi:10.1016/j.bpj.2016.07.005
26. Tristani-Firouzi, M. & Sanguinetti, M. C. Voltage-dependent inactivation of the human K⁺ channel KvLQT1 is eliminated by association with minimal K⁺ channel (minK) subunits. *J. Physiol.* (1998). doi:10.1111/j.1469-7793.1998.037bz.x
27. Alenghat, F. J. & Golan, D. E. Membrane protein dynamics and functional implications in mammalian cells. in *Current Topics in Membranes* (2013). doi:10.1016/B978-0-12-417027-8.00003-9
28. Manzo, C. & Garcia-Parajo, M. F. A review of progress in single particle tracking: From methods to biophysical insights. *Reports on Progress in Physics* (2015). doi:10.1088/0034-4885/78/12/124601
29. Brachet, A. *et al.* Ankyrin G restricts ion channel diffusion at the axonal initial segment before the establishment of the diffusion barrier. *J. Cell Biol.* (2010). doi:10.1083/jcb.201003042
30. Hedde, P. N., Staaf, E., Singh, S. B., Johansson, S. & Gratton, E. Pair Correlation Analysis Maps the Dynamic Two-Dimensional Organization of Natural Killer Cell Receptors at the Synapse. *ACS Nano* (2019). doi:10.1021/acsnano.9b07486
31. Malacrida, L., Hedde, P. N., Ranjit, S., Cardarelli, F. & Gratton, E. Visualization of barriers and obstacles to molecular diffusion in live cells by spatial pair-cross-correlation in two dimensions. *Biomed. Opt. Express* (2018). doi:10.1364/boe.9.000303
32. Malacrida, L., Rao, E. & Gratton, E. Comparison between iMSD and 2D-pCF analysis for molecular motion studies on in vivo cells: The case of the epidermal growth factor receptor. *Methods* (2018). doi:10.1016/j.ymeth.2018.01.010
33. Um, S. Y. & McDonald, T. V. Differential association between HERG and KCNE1 or KCNE2. *PLoS One* (2007). doi:10.1371/journal.pone.0000933
34. Chandrasekhar, K. D., Bas, T. & Kobertz, W. R. KCNE1 subunits require co-assembly with K⁺ channels for efficient trafficking and cell surface expression. *J. Biol. Chem.* (2006). doi:10.1074/jbc.M604398200
35. Chen, H., Kim, L. A., Rajan, S., Xu, S. & Goldstein, S. A. N. Charybdotoxin binding in the IKs pore demonstrates two MinK subunits in each channel complex. *Neuron* (2003). doi:10.1016/S0896-6273(03)00570-1
36. Wang, K. W. & Goldstein, S. A. N. Subunit composition of minK potassium channels. *Neuron* (1995). doi:10.1016/0896-6273(95)90277-5
37. Solé, L. *et al.* Functional Consequences of the Variable Stoichiometry of the Kv1.3-KCNE4 Complex. *Cells* (2020). doi:10.3390/cells9051128
38. Lussier, Y. *et al.* Disease-linked mutations alter the stoichiometries of HCN-KCNE2 complexes. *Sci. Rep.* (2019). doi:10.1038/s41598-019-45592-3
39. Manville, R. IV & Abbott, G. W. Potassium channels act as chemosensors for solute transporters. *Commun. Biol.* (2020). doi:10.1038/s42003-020-0820-9
40. Panaghie, G. & Abbott, G. The Impact of Ancillary Subunits on Small-Molecule Interactions with Voltage-Gated Potassium Channels. *Curr. Pharm. Des.* (2006). doi:10.2174/138161206777585175
41. Hu, Z. *et al.* Kcne3 deletion initiates extracardiac arrhythmogenesis in mice. *FASEB J.* (2014). doi:10.1096/fj.13-241828
42. Hu, Z., Crump, S. M., Zhang, P. & Abbott, G. W. Kcne2 deletion attenuates acute post-ischaemia/reperfusion myocardial infarction. *Cardiovasc. Res.* (2016). doi:10.1093/cvr/cvw048
43. Hu, Z. *et al.* Kcne2 deletion creates a multisystem syndrome predisposing to sudden cardiac death. *Circ. Cardiovasc. Genet.* (2014). doi:10.1161/CIRCGENETICS.113.000315
44. McCrossan, Z. A. & Abbott, G. W. The MinK-related peptides. *Neuropharmacology* (2004). doi:10.1016/j.neuropharm.2004.06.018
45. Roepke, T. K. *et al.* The KCNE2 potassium channel ancillary subunit is essential for gastric acid secretion. *J. Biol. Chem.* (2006). doi:10.1074/jbc.M604155200
46. Roepke, T. K. *et al.* Genetic dissection reveals unexpected influence of β subunits on KCNQ1 K⁺ channel polarized trafficking in vivo. *FASEB J.* (2011). doi:10.1096/fj.10-173682
47. Roepke, T. K. *et al.* Kcne2 deletion uncovers its crucial role in thyroid hormone biosynthesis. *Nat. Med.* (2009). doi:10.1038/nm.2029
48. Roepke, T. K. *et al.* Targeted deletion of kcne2 impairs ventricular repolarization via disruption of I_{K,slow1} and I_{to,f}. *FASEB J.* (2008). doi:10.1096/fj.08-110171
49. Roepke, T. K. *et al.* Targeted deletion of Kcne2 causes gastritis cystica profunda and gastric neoplasia. *PLoS One* (2010). doi:10.1371/journal.pone.0011451
50. Crump, S. M. & Abbott, G. W. Arrhythmogenic KCNE gene variants: Current knowledge and future challenges. *Frontiers in*

Genetics (2014). doi:10.3389/fgene.2014.00003

51. Sabater-Lleal, M. *et al.* Common genetic determinants of lung function, subclinical atherosclerosis and risk of coronary artery disease. *PLoS One* (2014). doi:10.1371/journal.pone.0104082
52. Wakil, S. M. *et al.* A genome-wide association study reveals susceptibility loci for myocardial infarction/coronary artery disease in Saudi Arabs. *Atherosclerosis* (2016). doi:10.1016/j.atherosclerosis.2015.11.019
53. Lee, S. M., Nguyen, D., Hu, Z. & Abbott, G. W. Kcne2 deletion promotes atherosclerosis and diet-dependent sudden death. *J. Mol. Cell. Cardiol.* (2015). doi:10.1016/j.yjmcc.2015.08.013
54. Lee, S. M. *et al.* Kcne2 deletion causes early-onset nonalcoholic fatty liver disease via iron deficiency anemia. *Sci. Rep.* (2016). doi:10.1038/srep23118
55. Salsbury, G. *et al.* Disruption of the potassium channel regulatory subunit KCNE2 causes iron-deficient anemia. *Exp. Hematol.* (2014). doi:10.1016/j.exphem.2014.07.269
56. Abbott, G. W. *et al.* KCNQ1, KCNE2, and Na⁺-coupled solute transporters form reciprocally regulating complexes that affect neuronal excitability. *Sci. Signal.* (2014). doi:10.1126/scisignal.2005025
57. Lee, S. M. *et al.* KCNE2 deletion impairs insulin secretion and causes type 2 diabetes mellitus. *FASEB J.* (2017). doi:10.1096/fj.201601347
58. Balse, E. & Boycott, H. E. Ion channel trafficking: Control of ion channel density as a target for arrhythmias? *Frontiers in Physiology* (2017). doi:10.3389/fphys.2017.00808
59. Dalal, R. B., Digman, M. A., Horwitz, A. F., Vetri, V. & Gratton, E. Determination of particle number and brightness using a laser scanning confocal microscope operating in the analog mode. *Microsc. Res. Tech.* (2008). doi:10.1002/jemt.20526

Figures

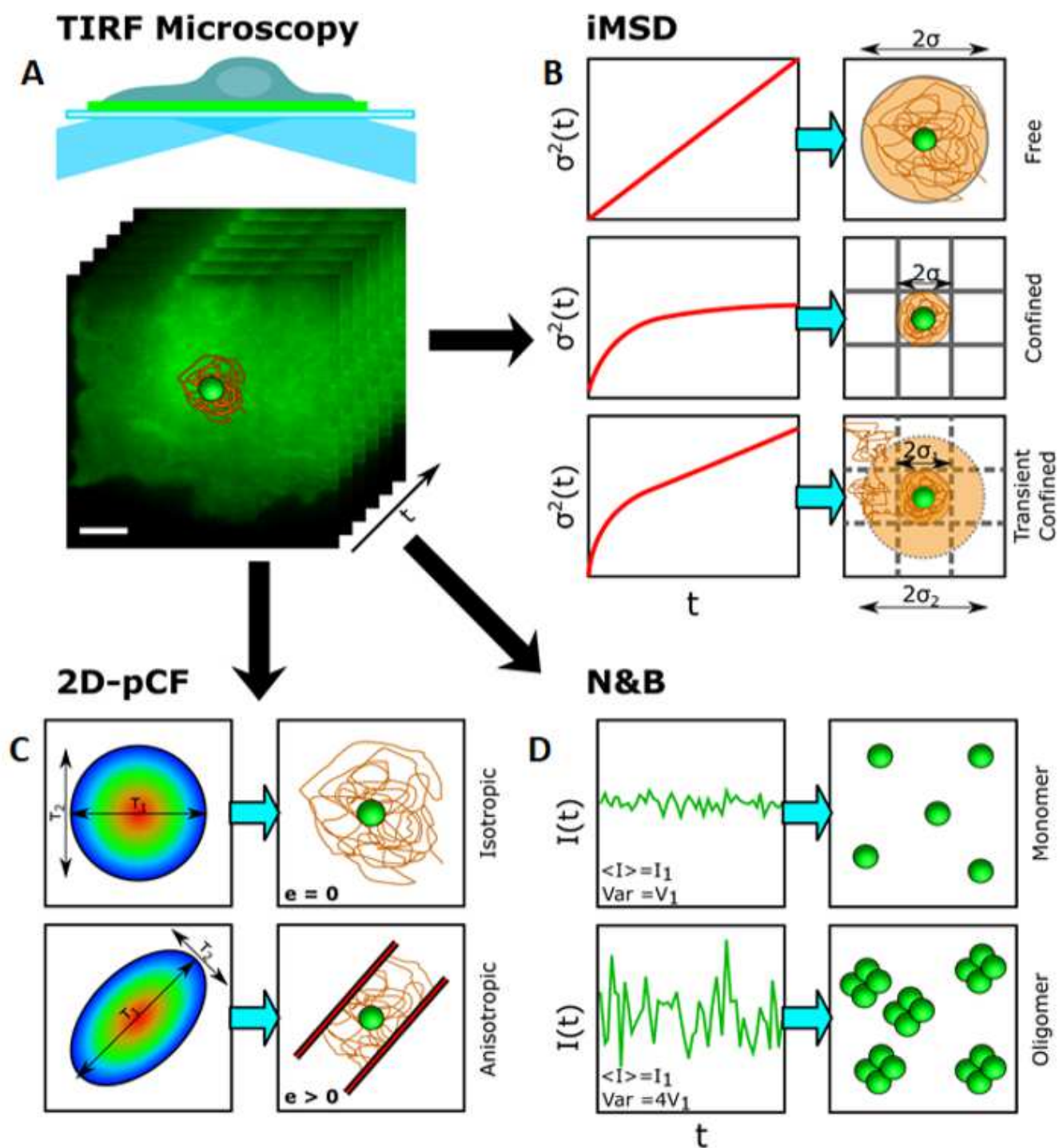


Figure 1

Schematic representation of the imaging and analysis approach. A: Image sequences are acquired using a TIRF microscope. B: Representative iMSD curves for different diffusion models (left) and their interpretation including free, confined and transient confined motions (right). C: Example of local 2D pair

correlation functions, 2D- pCF, (left) and their interpretation of either isotropic or anisotropic diffusion (right). D: Temporal fluorescence fluctuation intensities for different oligomerization states (left) and their interpretation (right) obtained from Number and Brightness analysis.

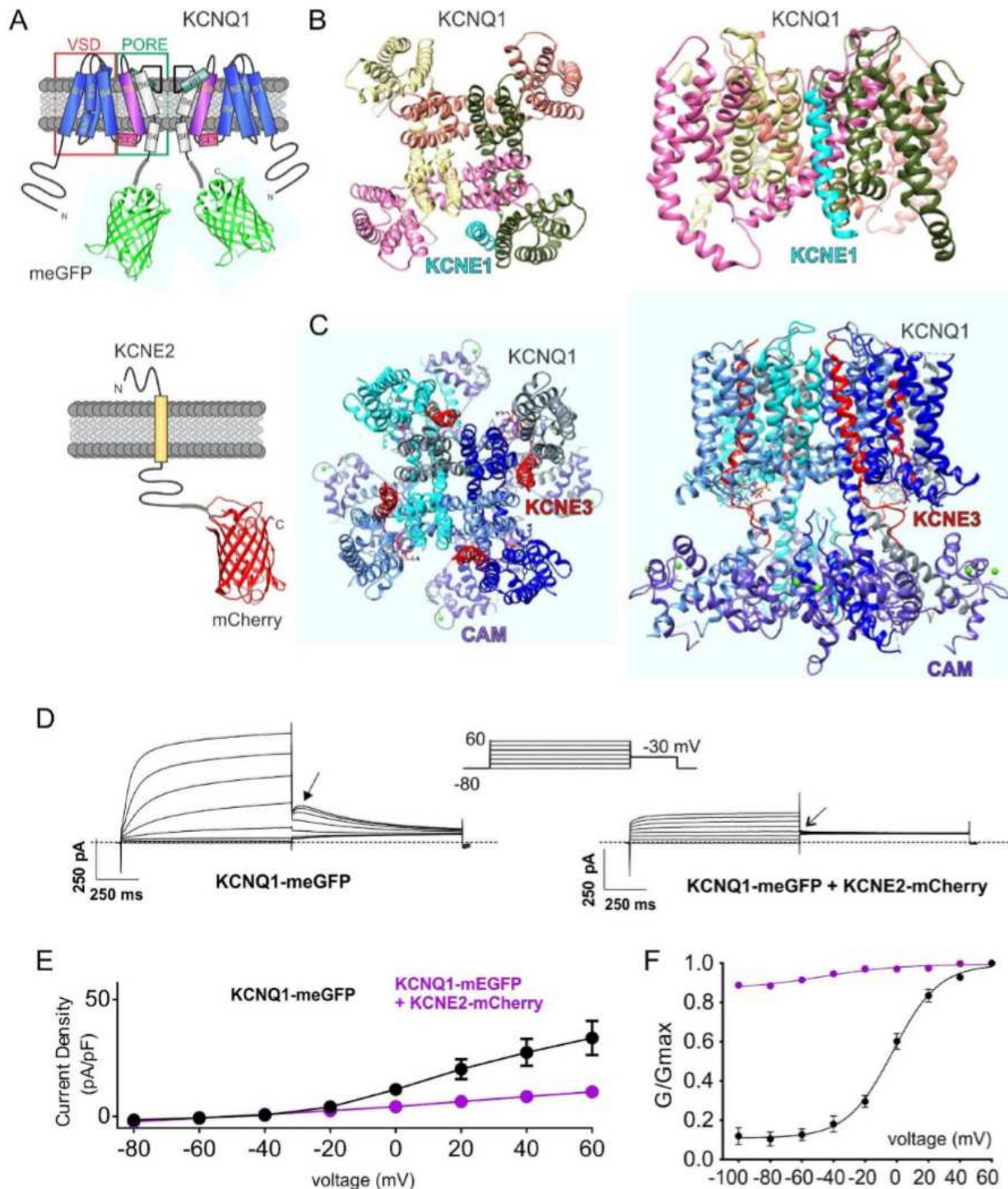


Figure 2

Fluorescent-tagged KCNQ1 and KCNQ1-KCNE2 express normal currents. A: Transmembrane topologies of KCNQ1 and KCNE2 subunits showing fluorescent protein tagging of the cytosolic domains. B:

Extracellular (left) and intramembrane (right) views of structural model of KCNQ1-KCNE1 complex⁵. C: Extracellular (left) and intramembrane (right) views of cryo-electron microscopy-resolved structure of KCNQ1-PIP2-KCNE3-calmodulin complex⁸. CAM = calmodulin. D: Exemplary traces showing whole-cell patch-clamp recordings from CHO cells transfected with the subunit combinations shown. Dotted line indicates zero current level. Upper inset shows the voltage protocol. Arrows indicate tail current features. E: Mean prepulse current density \pm SEM for currents expressed by KCNQ1-meGFP alone (black) ($n = 14$) or with KCNE2-mCherry (purple) ($n = 12$). F: Mean G/G_{max} relationship \pm SEM measured from tail currents at arrows in panel D for currents expressed by KCNQ1-meGFP alone (black) ($n = 14$) or with KCNE2-mCherry (purple) ($n = 12$).

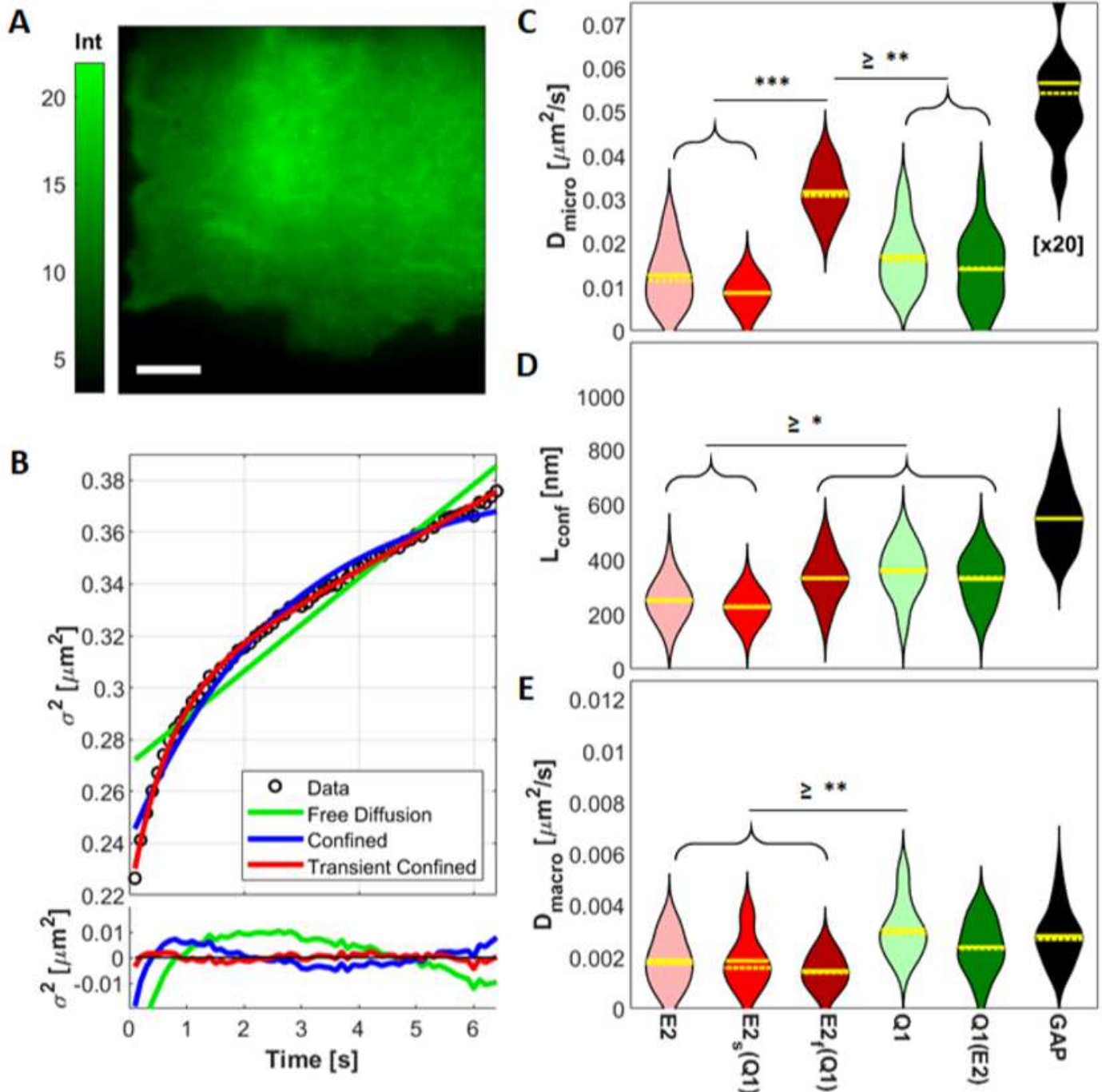


Figure 3

Representative average intensity image (A) and iMSD analysis (B) of a CHO cell transfected with KCNE2-meGFP. iMSD curve (B, top) fitted with three different diffusion models and their residuals (B, bottom). Violin plots of the parameters obtained from the fitting with a transient confined model: Dmicro (C), Lconf (D) and Dmacro (E) for the samples considered. Scale bar in A is 5 μm . Solid and dashed yellow lines represent the mean and the median of the distributions, respectively. Asterisks represent p-values <0.05 (*), <0.01 (**) and <0.001 (***).

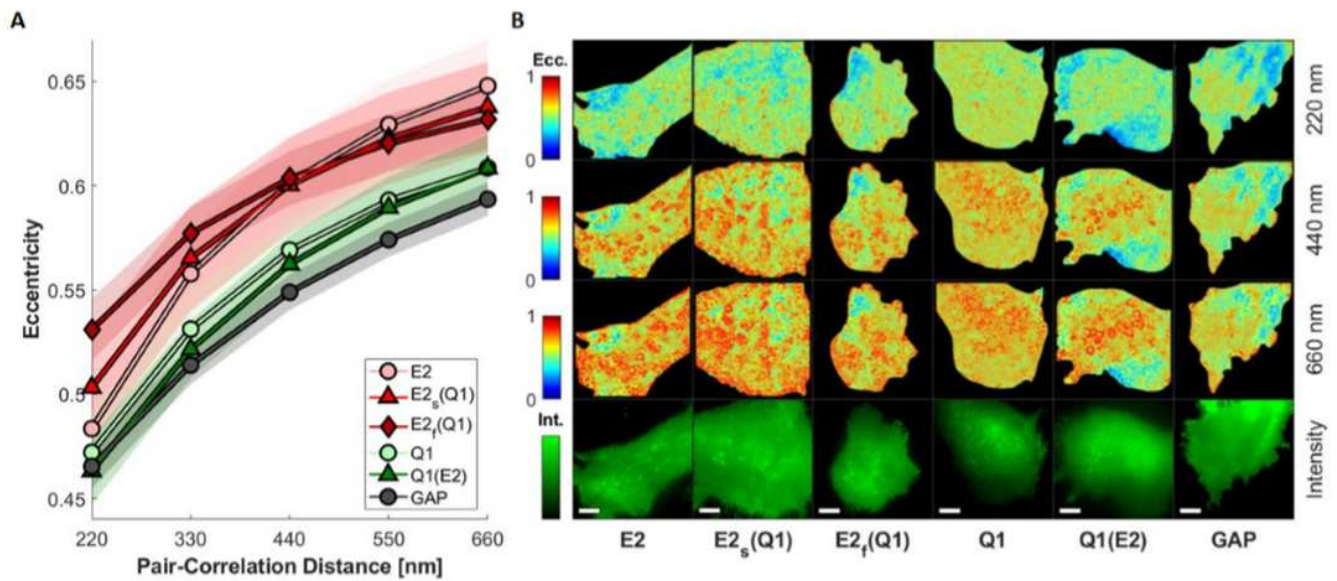


Figure 4

Median eccentricity as a function of the pCF distance considered (A), shaded areas represent the 95% confidence interval. B: Representative 2D-pCF eccentricity images computed at different distances and relative intensity images (bottom). Scale bar is 5 μm .

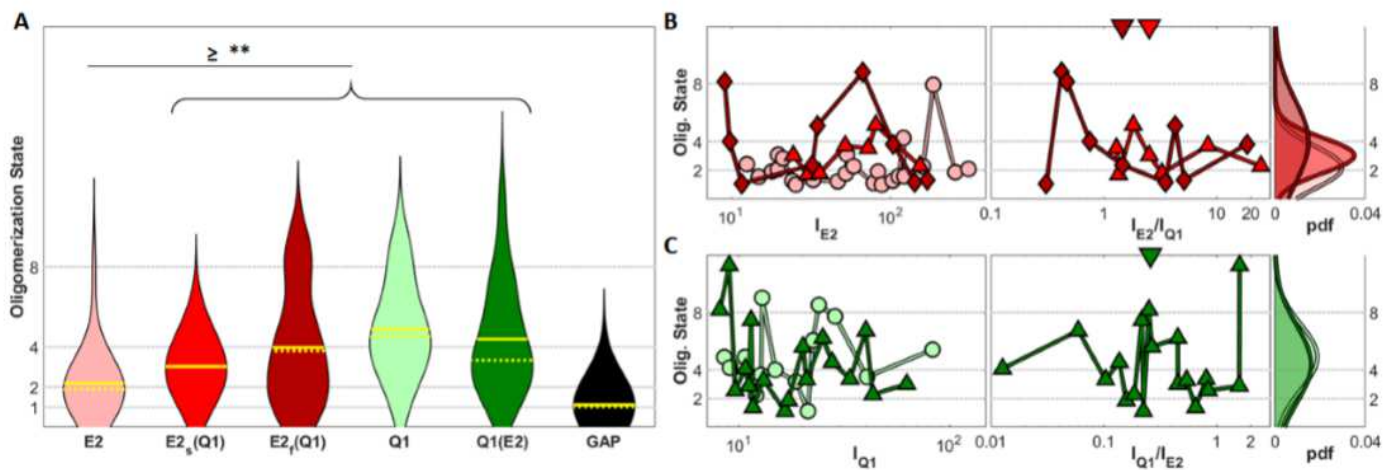


Figure 5

Violin plot for the oligomerization state as obtained by N&B analysis (A) for the samples considered. Dependence of the oligomerization state for the KCNE2-meGFP (B) and KCNQ1-meGFP (C) samples with the expression (left, represented by the average intensity of the meGFP channel) or co-expression (center, represented as the ratio between the average intensity of the meGFP and the mCherry channels) level, together with the corresponding probability density functions (right). Downward facing triangles in B and C represent the median co-expression level. Asterisks represent p-values <0.05 (*), <0.01 (**), and <0.001 (***). Colors and markers are the same as in Figure 4.

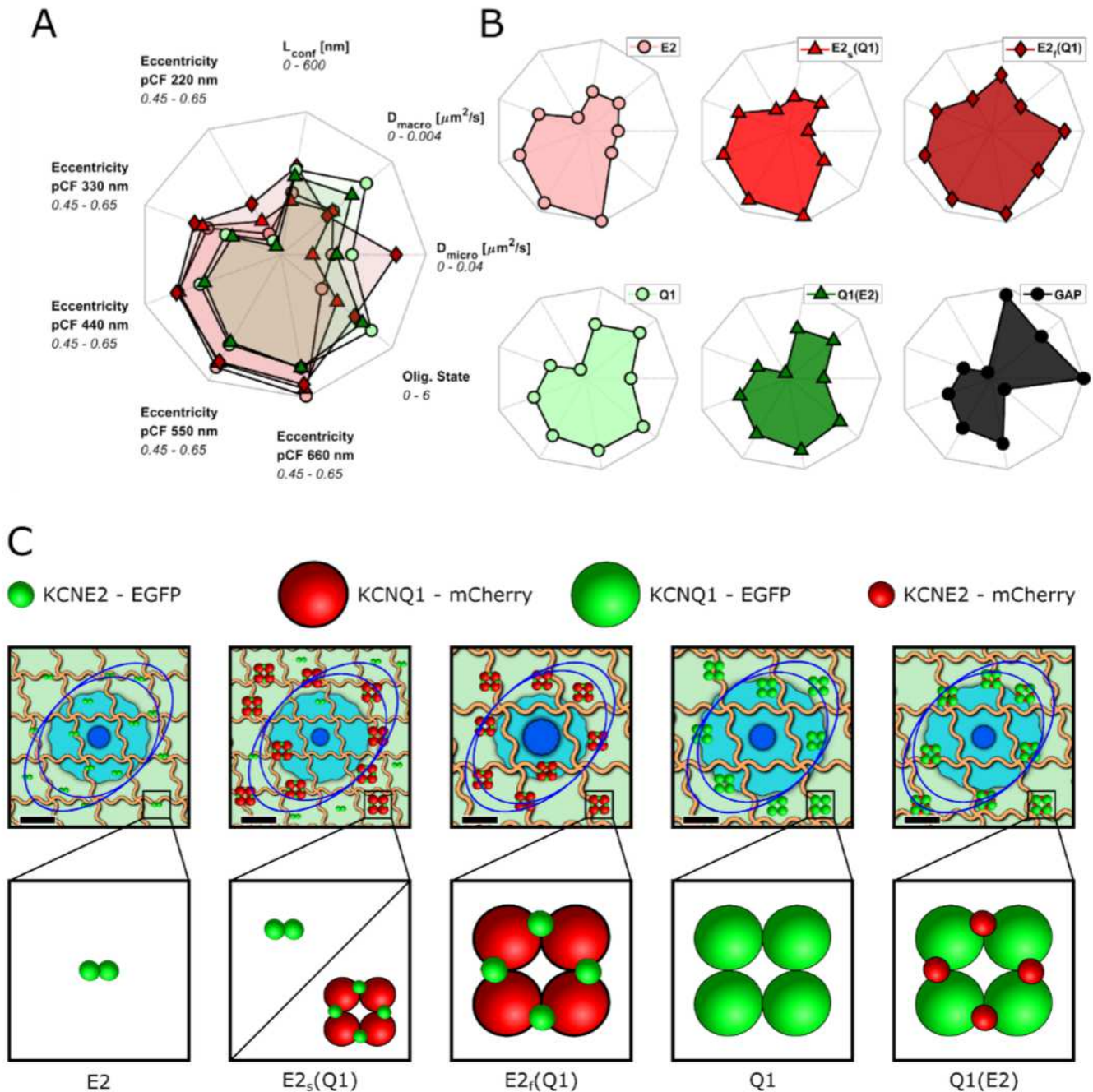


Figure 6

Combined (A) and individual (B) spider plots for all the conditions considered. C: Comprehensive schematic representation of the diffusional nano-environment together with the model of the oligomerization state for the KCNQ1-KCNE2 complex. Scale bar for the model is 200 nm and proteins are shown 10x their actual size. The dark blue and light blue circles represent the area covered by the diffusion of the protein in 0.5 s (calculated from Dmicro) and 60 s (calculated from Dmacro), respectively. Orange lines represent the nanodomains and the blue ellipses show the eccentricity as short scale (220 nm, internal ellipse) and long scale (660 nm, external ellipse).

Supplementary Files

This is a list of supplementary files associated with this preprint. Click to download.

- [SupplementaryFiguresScientificReports.pdf](#)